



ELSEVIER

Contents lists available at ScienceDirect

Mechanics of Materials

journal homepage: www.elsevier.com/locate/mechmat

A shear-lag model with a cohesive fibre–matrix interface for analysis of fibre pull-out

Zuorong Chen ^{a,*}, Wenyi Yan ^b^a CSIRO Energy Flagship, Private Bag 10, Clayton South, Victoria 3168, Australia^b Department of Mechanical and Aerospace Engineering, Monash University, Wellington Road, Clayton, Victoria 3800, Australia

ARTICLE INFO

Article history:

Received 18 February 2015

Received in revised form 26 May 2015

Available online 17 July 2015

Keywords:

Shear-lag model

Cohesive interface

Interfacial debonding

Fibre pull-out

ABSTRACT

A shear-lag model with a cohesive fibre–matrix interface has been developed for the analysis of stress transfer between the fibre and the matrix in fibre-reinforced composites in this paper. A bilinear cohesive damage evolution law is used to describe the fibre–matrix interface behaviour. The governing equations for the interfacial shear stress and the axial stress in the fibre are derived. Accurate analytical solutions are obtained when the fibre–matrix interface is in the initial linear elastic deformation regime. When debonding occurs, interfacial damage and softening are modelled by superposing two elastic stress systems and satisfying the damage evolution law at both ends of the damage process zone, and approximate analytical solutions are obtained. The stress distribution and evolution during the fibre pull-out, the maximum pull-out force and the pull-out curve have been analysed using a shear strength-based debonding criterion. Analytical expressions for the maximum fibre pull-out force and its limit as the embedded fibre length approaches infinity are obtained. In addition, the new function proposed for describing the radial distribution of the shear stress in the matrix fixes the problem of zero shear-lag parameter when b/a approaches infinity, enabling the shear-lag analysis to deal with low fibre volume fractions. Generally, the analytical solutions compare satisfactorily well to the cohesive finite element calculations and experimental data in the literature.

© 2015 Elsevier Ltd. All rights reserved.

1. Introduction

The load transfer mechanism between the fibre and the matrix and the fibre–matrix interface behaviour play an important role in determining the mechanical properties of fibre-reinforced composites such as elastic modulus, tensile strength and fracture toughness, and have received considerable attention and extensive investigations. Tensile stresses acting on the composites can be transferred between the matrix and fibres by shear at the fibre–matrix interface. Theoretical analysis of the load transfer and interfacial debonding problem during fibre

pull-out can be classified into two principal approaches; one is the strength-based approach where the interfacial debonding takes place when the interfacial shear stress reaches the interfacial strength (Cox, 1952; Hsueh, 1988, 1992; Landis and McMeeking, 1999; Lawrence, 1972; Leung and Li, 1991; McCartney, 1992; Nairn, 1997, 2004; Nayfeh, 1977), and the other is the fracture mechanics-based approach where the interfacial debonding is treated as a mode II fracture which propagates once the interfacial toughness is overcome (Budiansky et al., 1986; Gao et al., 1988; Gurney and Hunt, 1967; Hutchinson and Jensen, 1990; Nairn, 2000; Stang and Shah, 1986; Zhou et al., 1992). The two theories of interfacial debonding and fibre pull-out have been compared experimentally (Kim et al., 1992; Zhandarov et al., 2001),

* Corresponding author. Tel.: +61 3 9545 8379; fax: +61 3 9545 8380.
E-mail address: zuorong.chen@csiro.au (Z. Chen).

and theoretically (Leung and Li, 1991; Stang et al., 1990), indicating the conditions of their validity.

In the strength-based theories, the original shear-lag theory (Cox, 1952) has been widely adopted to obtain the shear stress distribution at the fibre–matrix interface. Modifications of the classical shear-lag model have been made to obtain improved results (Hsueh, 1992; McCartney, 1989; Nairn, 1997, 2004; Nayfeh and Abdelrahman, 1998). Extensions of the shear-lag model with introducing interfacial friction have been proposed to analyse interfacial debonding during the fibre pull-out or push-out (Budiansky et al., 1986; Leung and Li, 1991; McCartney, 1989; Shetty, 1988; Zhou et al., 1993).

Recently, owing to their extraordinary physical and mechanical properties such as high tensile stiffness and strength and low density, carbon nanotubes (CNTs) find promising applications as reinforcements in advanced structural composites. Early experimental measurements showed very disappointing improvements in the mechanical properties of carbon nanotube based composites. It has been identified through both experimental and numerical studies that the CNT-matrix interfacial characteristics (interfacial strength and length) critically control the performance of such composites and therefore they have attracted considerable attention of many researchers. Various interfacial interaction models have been adopted in analysis of the stress transfer between carbon nanotube and matrix. For examples, the van der Waals interfacial interaction between the polymer matrix and the CNT and the interfacial chemical bonding have been modelled with the Lennard-Jones potential, and the many-body bond-order potential, respectively, in analysis of the shear strength of carbon nanotube-polymer matrix interfaces (Chen et al., 2010; Frankland et al., 2002, 2003). Nonlinear cohesive laws for CNT-polymer matrix interfaces have been established based on the van der Waals interfacial interaction (Jiang et al., 2006; Lu et al., 2008) and chemical bonding (Jiang, 2010), respectively. The classical shear-lag model has been adopted to predict the interfacial stress transfer in CNT-reinforced polymer composites (Gao and Li, 2005), to analyse the carbon nanotube pull-out from a polymer matrix (Frankland and Harik, 2003), and to investigate fracture toughness enhancement with introducing a linear interface law to account for CNT-matrix interfacial bond breaking (Chen et al., 2010). The shear-lag model has also been used to analyse the pull-out test of CNT-coated carbon fibres in a polyester matrix (Agnihotri et al., 2012), and cohesive zone finite element models have been established with introducing a non-linear interface cohesive law to model the pull-out response of CNT-coated fibres (Agnihotri et al., 2012; Jia et al., 2014).

The development of cohesive laws for characterising the CNT-matrix interfacial properties, and the application of different cohesive laws together with the classical shear-lag theory in analysing the load transfer between CNT and matrix inspire us to establish an analytical relationship between the load transfer and evolution and the interfacial cohesive properties. We first derive the governing equations for a shear-lag model with a cohesive fibre–matrix interface by introducing an interfacial bilinear

cohesive law into the classical shear-lag model in Section 2. The accurate analytical solution for the cohesive interface in the initial linear elastic deformation regime is given in Section 3. In Section 4, we propose a simple method to obtain approximate analytical solutions when interfacial damage and softening occur. The analytical solutions for the distribution and evolution of the interfacial shear stress and axial stress in the fibre are compared to the cohesive zone finite element calculations and experimental data available in the literature.

2. A shear-lag model with a cohesive fibre–matrix interface

A composite cylinder shear-lag model is adopted for the analysis of the load transfer from the fibre to the matrix when the fibre is loaded. As shown in Fig. 1, a single fibre with a radius a is embedded with a length L in a coaxial matrix cylinder with an outer radius b . The fibre is subjected to an axial tensile stress σ_p at the loaded end ($z = L$). The embedded end face ($z = 0$) between the fibre and matrix can be perfectly bonded or completely free. It is assumed that both the fibre and matrix are elastic, and the interface transfers stresses between the fibre and matrix by interfacial shear. The outer surface ($r = b$) is stress-free.

The interface ($r = a$) between the fibre and matrix is modelled as a cohesive interface in pure shear mode. The shear behaviour of the cohesive interface is described by a bilinear cohesive traction-separation law, as shown in Fig. 2. The cohesive law is characterised by an initial linear elastic regime followed by a linear softening regime. Interfacial damage initiates once the interfacial shear stress reaches the cohesive strength τ_0 and the shear separation reaches the critical value δ_0 . Beyond this point, as the shear separation increases further, the shear stress decreases due to material degradation until the complete failure (interfacial debonding) begins where the separation reaches the critical value δ_1 and the traction or cohesive strength acting across the cohesive interface is reduced to zero.

The bilinear cohesive traction-separation constitutive relation is given by

$$\tau = \begin{cases} K_0\delta & \text{if } 0 \leq \delta^{max} \leq \delta_0 \\ (1 - D)K_0\delta & \text{if } \delta_0 \leq \delta^{max} \leq \delta_1 \\ 0 & \text{if } \delta^{max} \geq \delta_1 \end{cases} \quad (1)$$

where K_0 is the initial shear stiffness of the cohesive interface, δ^{max} is the maximum value of the shear separation attained during the fibre pull-out, and D is the scalar damage variable.

This law assumes that the cohesive surfaces initially are intact without any relative displacement, and exhibit reversible linear elastic behaviour until the traction reaches the cohesive strength τ_0 or equivalently the separation exceeds δ_0 . Beyond δ_0 , the traction reduces linearly to zero up to δ_1 and any unloading takes place irreversibly. The area under the traction-separation curve represents the fracture energy, G_c , of the cohesive crack.

In this paper, a cohesive interface between the fibre and matrix is modelled, so there is a displacement discontinuity (or jump) cross the interface ($r = a$). The axial displacement of the fibre and matrix at $r = a$ and the shear separation (δ) of the cohesive interface satisfy the following deformation relation

$$w^f(a, z) - w^m(a, z) = \delta(z) \quad (8)$$

This axial displacement discontinuity relation has been implemented into shear-lag analysis for imperfect interface modelling (Nairn, 2004).

Following the approach (Nayfeh, 1977), the average of any variable $f(r, z)$ over the cross-sectional area ($r_i \leq r \leq r_o$) is defined as

$$\bar{f}(z) = \frac{1}{\pi(r_o^2 - r_i^2)} \int_{r_i}^{r_o} 2\pi r f(r, z) dr \quad (9)$$

Applying Eq. (9) to Eq. (4) over the fibre ($0 \leq r \leq a$) and the matrix ($a \leq r \leq b$), respectively, leads to the results

$$\frac{d\bar{\sigma}_{zz}^f(z)}{dz} = -\frac{2\tau_{rz}^f(a, z)}{a} = -\frac{2\tau_a(z)}{a} \quad (10)$$

$$\frac{d\bar{\sigma}_{zz}^m(z)}{dz} = \frac{2\tau_{rz}^m(a, z)}{(b^2 - a^2)/a} = \frac{2\tau_a(z)}{(b^2 - a^2)/a} \quad (11)$$

$$\frac{d^2\bar{\sigma}_{zz}^f(z)}{dz^2} = \frac{\left[\frac{1}{\left(\frac{b^2}{a^2} - 1 \right)} + \frac{E_A^m}{E_A^f} \right]}{a^2 E_A^m \left\{ \frac{r}{4G_A^f} + \frac{[(b^2/r^2 - 1)rO(r)]}{4G_A^m} \right\}} \left\{ \bar{\sigma}_{zz}^f(z) - \frac{\sigma_p}{\left[1 + \left(\frac{b^2}{a^2} - 1 \right) \frac{E_A^m}{E_A^f} \right]} - \frac{E_A^m \left(\frac{b^2}{a^2} - 1 \right)}{\left[1 + \left(\frac{b^2}{a^2} - 1 \right) \frac{E_A^m}{E_A^f} \right]} \left[\frac{d\delta(z)}{dz} + (\alpha_A^m - \alpha_A^f) T \right] \right\} \quad (19)$$

Multiplying Eq. (3) by r^2 , substituting Eqs. (5)₂ and (6)₁, and then integrating with respect to r over the cross-sectional area of the fibre ($0 \leq r \leq a$) yields

$$w^f(a, z) - \bar{w}^f(z) = \frac{\tau_a(z)}{2G_A^f} \overline{r} \quad (12)$$

Similarly, multiplying Eq. (3) by $(b^2 - r^2)$, substituting Eqs. (5)₂ and (6)₂, and then integrating with respect to r over the cross-sectional area of the matrix ($a \leq r \leq b$) yields

$$\bar{w}^m(z) - w^m(a, z) = \frac{\tau_a(z)}{2G_A^m} \overline{[(b^2/r^2 - 1)rO(r)]} \quad (13)$$

The addition of Eqs. (12) and (13), using the relation equation (8), yields

$$\bar{w}^m(z) - \bar{w}^f(z) + \delta(z) = \left\{ \frac{r}{2G_A^f} + \frac{[(b^2/r^2 - 1)rO(r)]}{2G_A^m} \right\} \tau_a(z) \quad (14)$$

Differentiate Eq. (14) with respect to z yields

$$\bar{e}_{zz}^m(z) - \bar{e}_{zz}^f(z) + \frac{d\delta(z)}{dz} = \left\{ \frac{r}{2G_A^f} + \frac{[(b^2/r^2 - 1)rO(r)]}{2G_A^m} \right\} \frac{d\tau_a(z)}{dz} \quad (15)$$

Averaging Eq. (2) by applying Eq. (9) over the fibre ($0 \leq r \leq a$) and the matrix ($a \leq r \leq b$), respectively, leads to the results

$$\bar{e}_{zz}^f(z) = \frac{\bar{\sigma}_{zz}^f(z)}{E_A^f} - \frac{\nu_A^f}{E_A^f} \left[\bar{\sigma}_{rr}^f(z) + \bar{\sigma}_{\theta\theta}^f(z) \right] + \alpha_A^f T$$

$$\bar{e}_{zz}^m(z) = \frac{\bar{\sigma}_{zz}^m(z)}{E_A^m} - \frac{\nu_A^m}{E_A^m} \left[\bar{\sigma}_{rr}^m(z) + \bar{\sigma}_{\theta\theta}^m(z) \right] + \alpha_A^m T \quad (16)$$

The outer surface boundary ($r = b$) is stress free, so the mechanical equilibrium condition leads to

$$a^2 \bar{\sigma}_{zz}^f(z) + (b^2 - a^2) \bar{\sigma}_{zz}^m(z) = a^2 \sigma_p \quad (17)$$

Using the assumption (McCartney, 1992; Nairn, 1997)

$$\left| \frac{\nu_A}{E_A} (\bar{\sigma}_{rr} + \bar{\sigma}_{\theta\theta}) \right| \ll \left| \frac{\bar{\sigma}_{zz}}{E_A} + \alpha_A T \right| \quad (18)$$

differentiating Eq. (10) and substituting it together with Eqs. (16) and (17) into Eq. (15) results in

The differential equations (19) and (10) together with the traction-separation cohesive law equation (1) constitute the governing equations for the shear-lag model with a cohesive fibre–matrix interface, from which the stress distributions can be derived when subjected to appropriate boundary conditions.

For clarity, the average of the axial tensile stress in the fibre, $\bar{\sigma}_{zz}^f(z)$, is represented by $\sigma_f(z)$ in the following analysis.

3. Solution for initial linear elastic regime

For the cohesive interface in the initial linear elastic regime, it can be obtained by differentiating Eq. (1) and making use of Eq. (10) that

$$\frac{d\delta(z)}{dz} = \frac{1}{K_0} \frac{d\tau(z)}{dz} = -\frac{1}{K_0} \frac{d\tau_a(z)}{dz} = \frac{a}{2K_0} \frac{d^2\sigma_f(z)}{dz^2} \quad (20)$$

where $\tau(z)$ is the shear traction in the cohesive interface, and $\tau(z) = -\tau_a(z)$.

On substituting Eq. (20) into Eq. (19) it can be shown that the average axial tensile stress in the fibre satisfies the following second order differential equations

$$\sigma_f = \sigma_p \varphi(\zeta, l, \alpha) \quad \tau_a = -\frac{\sigma_p}{2} \omega(\zeta, l, \alpha) \quad \delta = \frac{\sigma_p}{2K_0} \omega(\zeta, l, \alpha) \tag{25}$$

$$\frac{d^2 \sigma_f(z)}{dz^2} = \frac{2 \left(\frac{a^2}{b^2 - a^2} + \frac{E_A^m}{E_A^f} \right)}{a^2 \left[\frac{E_A^m}{2G_A^f} \left[\frac{r}{a} I(r) \right] + \frac{E_A^m}{2G_A^m} \left[\left(\frac{b^2}{r^2} - 1 \right) \frac{r}{a} O(r) \right] + \frac{E_A^m}{aK_0} \right]} \left\{ \sigma_f(z) - \frac{1}{\left[1 + \frac{E_A^m}{E_A^f} \left(\frac{b^2}{a^2} - 1 \right) \right]} \sigma_p - \sigma_T \right\} \tag{21}$$

where $\sigma_T = \frac{E_A^m (\alpha_A^m - \alpha_f^f) T}{\frac{a^2}{b^2 - a^2} + \frac{E_A^m}{E_A^f}}$

Let us now introduce the following scaling parameters:

$$\zeta = z/a, \quad l = L/a,$$

$$\alpha = \left\{ \frac{2 \left[\frac{1}{(b^2/a^2 - 1)} + \frac{E_A^m}{E_A^f} \right]}{\frac{E_A^m}{2G_A^f} \left[\frac{r}{a} I(r) \right] + \frac{E_A^m}{2G_A^m} \left[\left(\frac{b^2}{r^2} - 1 \right) \frac{r}{a} O(r) \right] + \frac{E_A^m}{aK_0}} \right\}^{1/2}, \quad \text{and}$$

$$\gamma = \frac{1}{\left[1 + \frac{E_A^m}{E_A^f} \left(\frac{b^2}{a^2} - 1 \right) \right]}$$

Then, the governing equation (21) can be expressed as:

$$\frac{d^2 \sigma_f(\zeta)}{d\zeta^2} = \alpha^2 [\sigma_f(\zeta) - \gamma \sigma_p - \sigma_T] \tag{22}$$

and the interfacial shear stress is

$$\tau_a(\zeta) = -\frac{1}{2} \frac{d\sigma_f(\zeta)}{d\zeta} \tag{23}$$

With a slight difference in the expression, Eq. (22) is essentially identical to the result obtained by Nairn (2004) in modelling imperfect interface with introducing an imperfect interface parameter into shear-lag analysis. The shear-lag parameter α is the same as that obtained by Nairn. The denominator of the shear-lag parameter α consists of three parts: the fibre term; the matrix term; and the cohesive interface term. For the case that the initial interfacial shear stiffness K_0 is far greater than E_A^m/a , the cohesive interface term disappears, the shear-lag parameter, α , and Eq. (22) are reduced to the result of the classical shear-lag model where a perfectly bonded fibre–matrix interface is assumed.

Define the following boundary conditions:

$$\sigma_f(\zeta = 0) = \epsilon \sigma_p, \quad \sigma_f(\zeta = l) = \sigma_p \tag{24}$$

where the dimensionless factor ϵ defines relation between the applied load, σ_p , and the average fibre axial stress at the embedded end face ($\zeta = 0$).

Solution of Eq. (22) subjected to the boundary conditions equation (24) yields, for the case of $\sigma_T = 0$,

where

$$\begin{aligned} \varphi(\zeta, l, \alpha) &= \frac{\text{Sinh}(\alpha\zeta)}{\text{Sinh}(\alpha l)} - \epsilon \frac{\text{Sinh}[\alpha(\zeta - l)]}{\text{Sinh}(\alpha l)} \\ &\quad + \gamma \left[1 - \frac{\text{Sinh}(\alpha\zeta) - \text{Sinh}[\alpha(\zeta - l)]}{\text{Sinh}(\alpha l)} \right] \\ \omega(\zeta, l, \alpha) &= \varphi'(\zeta, l, \alpha) = \alpha \left\{ \frac{\text{Cosh}(\alpha\zeta)}{\text{Sinh}(\alpha l)} - \epsilon \frac{\text{Cosh}[\alpha(\zeta - l)]}{\text{Sinh}(\alpha l)} \right. \\ &\quad \left. - \gamma \frac{\text{Cosh}(\alpha\zeta) - \text{Cosh}[\alpha(\zeta - l)]}{\text{Sinh}(\alpha l)} \right\} \end{aligned} \tag{26}$$

For the case of a completely free fibre end face at $\zeta = 0$, we have $\epsilon = 0$. For the case that the fibre end face at $\zeta = 0$ is fully bonded with the matrix, it is generally difficult to define the exact boundary condition, but various treatments are available to provide good approximate boundary conditions (Clyne, 1989; Hsueh, 1988, 1992; Starink and Syngellakis, 1999). So, Eq. (25) provides unified expressions for the solutions for both the completely free ($\epsilon = 0$) and fully bonded ($\epsilon \neq 0$) fibre end faces. As the initial shear stiffness of the cohesive interface, K_0 , approaches infinity, the shear separation δ in Eq. (25) is zero, and Eq. (25) is reduced to the solution of the classical shear-lag model (Hsueh, 1988, 1992).

Analysis of the terms of Eq. (25) provides insight into the characteristics of the solution. The first term $\frac{\text{Sinh}(\alpha\zeta)}{\text{Sinh}(\alpha l)}$ in $\varphi(\zeta, l, \alpha)$ is equal to 0 at $\zeta = 0$ and 1 at $\zeta = l$, the second term $-\frac{\text{Sinh}[\alpha(\zeta - l)]}{\text{Sinh}(\alpha l)}$ is equal to 1 at $\zeta = 0$ and 0 at $\zeta = l$, and the third term is equal to 0 at both $\zeta = 0$ and $\zeta = l$ and 1 at $\zeta = l/2$, symmetric with respect to $\zeta = l/2$. So, the first term represents the effect of the load, the second term reflects the effect of the boundary conditions at the embedded fibre end face ($\zeta = 0$), and the third term describes the effect of γ on the axial stress distribution in the fibre ($0 < \zeta < l$).

Different assumptions on the radial dependence of the shear stress in the fibre and matrix have been adopted in shear-lag models. The assumption of $I(r) = 0$ and $O(r) = a/r$ (Aveston and Kelly, 1973; Budiansky et al., 1986; Cox, 1952; Hsueh, 1988) ignores the shear stress in the fibre and does not strictly satisfy the stress-free boundary condition at the outer surface ($r = b$). Improved results have been obtained by assuming $I(r) = r/a$ and

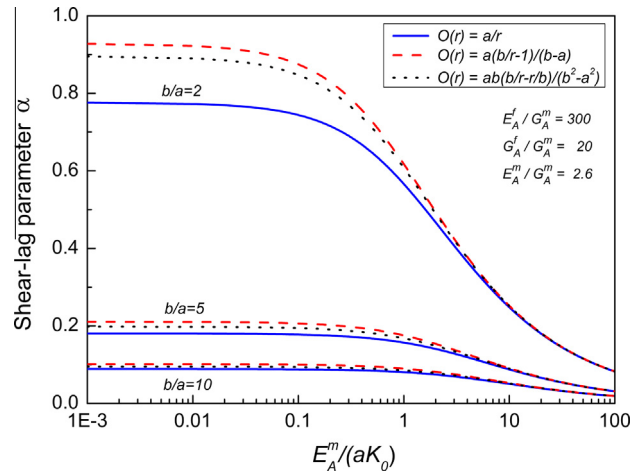


Fig. 3. The dimensionless shear-lag parameter α as a function of $E_A^m/(aK_0)$.

$O(r) = ab(b/r - r/b)/(b^2 - a^2)$ (McCartney, 1989; Nairn, 1997, 2004; Nayfeh, 1977) which satisfies the interface continuity and boundary conditions for the shear stress. Fig. 3 compares the shear-lag parameter α as a function of $E_A^m/(aK_0)$ for different b/a by using three different forms of the radial dependence function $O(r)$. It is shown that the difference between the three expressions decreases as the ratio $E_A^m/(aK_0)$ increases, and is insignificant for a large b/a .

It has been shown that the shear-lag method does not work for low fibre volume fractions because the shear-lag parameter α approaches zero as b/a becomes large (Nairn, 1997). This limitation arises from a term of $\ln(b/a)$ in the matrix term of the dominator that approaches infinity as b/a approaches infinity. To fix this problem, modification has been made by adding a small constant χ to $\ln(b/a)$ to replace it with $-\ln\sqrt{a^2/b^2 + \chi}$ in a generalised shear-lag analysis (Nairn, 2004). $\chi = 0.009$ has been suggested by best fitting finite element results.

For a shear-lag analysis to be applicable when b/a becomes large, the function $O(r)$ needs to satisfy the condition that the average $\left[\left(\frac{b^2}{r^2} - 1\right) \frac{r}{a} O(r)\right]$ converges as b/a approaches infinity. Actually, the average $\left[\left(\frac{b^2}{r^2} - 1\right) \frac{r}{a} O(r)\right]$ in the dominator of the shear-lag parameter always includes the $\ln(b/a)$ term if the assumed function $O(r)$ has a $1/r$ term. So the choice of an appropriate function $O(r)$ without $1/r$ term may overcome this limitation. In this paper, the radial dependence function $O(r)$ is defined as

$$O(r) = \frac{e^{\lambda(b-r)/a} - 1}{e^{\lambda(b-a)/a} - 1} \quad (27)$$

where the positive constant λ describes the rate at which the shear stress changes with respect to the radial distance.

Eq. (27) satisfies the interfacial and boundary conditions equation (7) and decays fast towards zero as r approaches b . Most important is that it results in a finite

average $\left[\left(\frac{b^2}{r^2} - 1\right) \frac{r}{a} O(r)\right]$ as b/a approaches infinity. It can be shown that

$$\lim_{b/a \rightarrow \infty} \left[\left(\frac{b^2}{r^2} - 1 \right) \frac{r}{a} \frac{e^{\lambda(b-r)/a} - 1}{e^{\lambda(b-a)/a} - 1} \right] = \frac{2}{\lambda} \quad (28)$$

which ensures a well defined shear-lag parameter at zero fibre volume fraction.

Fig. 4 compares the different radial dependence functions for the shear stress, together with the finite element analysis results. For comparison, an axisymmetrical finite element model has been established to model the fibre pull-out by using the commercial finite element package ABAQUS. The geometric model and parameters for the finite element modelling are given in the inset of Fig. 4. Axisymmetrical elements (CAX4) are used to model the fibre and matrix, and zero-thickness cohesive elements (COHAX4) are used to model the cohesive fibre–matrix interface. The axial displacement at the bottom boundary of the matrix is constrained. The bottom end face of the fibre is free from the matrix. Uniform displacement load is applied to the top end face of the fibre. The radial dependence function equation (27) with $\lambda = 0.45$ is much closer to the finite element results, and is used in the following analysis. For $\lambda = 0.62$, Eq. (28) yields a limit of 3.23, which is very close to Nairn's result of $-\ln 0.009 - 3/2 = 3.21$ at zero fibre volume fraction (Nairn, 2004).

The “exact” shear-lag stress state has been given by Nairn (1997). For an approximate shear-lag analysis, as it is shown in the generalised shear-lag analysis (Nairn, 2004), there are an infinite number of functions that can be used to approximate the radial dependence of the shear stress. For example, the following function may also provide a good approximation to the radial distribution

$$O(r) = \frac{a^s b^s}{b^{2s} - a^{2s}} \left(\frac{b^s}{r^s} - \frac{r^s}{b^s} \right) \quad (29)$$

which satisfies the interfacial and boundary conditions equation (7) and decays towards zero as r approaches b . It can be shown that, for $s > 1$,

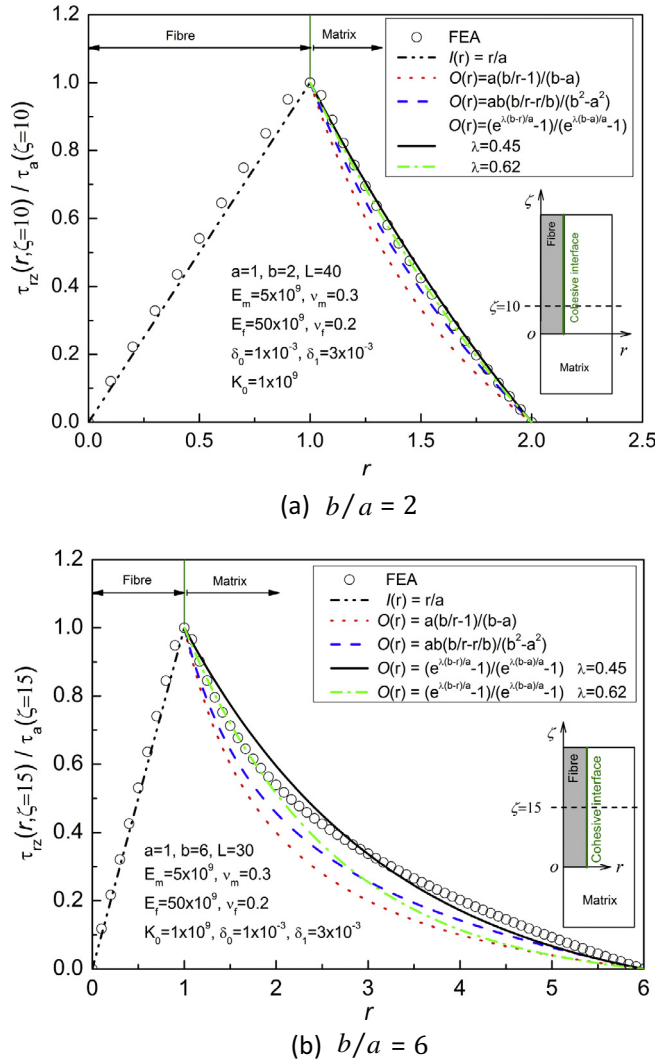


Fig. 4. Comparison of different radial dependence functions for the shear stress: (a) $b/a = 2$; and (b) $b/a = 6$.

$$\lim_{b/a \rightarrow \infty} \left[\left(\frac{b^2}{r^2} - 1 \right) \left(\frac{r}{a} \right) \frac{a^s b^s}{b^{2s} - a^{2s}} \left(\frac{b^s}{r^s} - \frac{r^s}{b^s} \right) \right] = \frac{2}{s-1} \quad (30)$$

In order for Eq. (29) or (27) to be used to approximate the radial dependence of the shear stress in a shear-lag analysis, an appropriately chosen parameter s in Eq. (29) or λ in Eq. (27) should provide a smooth transition between results for large and small b/a and work for any combination of real fibre and matrix properties (Nairn, 2004).

Comparison of the magnitude of the cohesive shear stresses at the embedded end ($\zeta = 0$) and the loaded end ($\zeta = l$) provides a criterion that determines at which end interfacial damage and thus debonding will initiate. The shear-strength based debonding criterion indicates that the interfacial damage and debonding will initiate at left end ($\zeta = 0$), at right end ($\zeta = l$), or at both ends,

respectively, if $|\tau(\zeta = 0)|$ is larger than, less than, or equal to $|\tau(\zeta = l)|$. It can be derived from Eq. (25) that, for the case of $\tau(\zeta = 0) > 0$ and $\tau(\zeta = l) > 0$,

$$\begin{aligned} \tau(\zeta = 0) > \tau(\zeta = l) & \quad \text{if } 2\gamma - \epsilon > 1 \\ \tau(\zeta = 0) = \tau(\zeta = l) & \quad \text{if } 2\gamma - \epsilon = 1 \\ \tau(\zeta = 0) < \tau(\zeta = l) & \quad \text{if } 2\gamma - \epsilon < 1 \end{aligned} \quad (31)$$

So, in this case, interfacial damage and debonding will initiate at the embedded end ($\zeta = 0$) if $2\gamma - \epsilon > 1$, at the loaded end ($\zeta = l$) if $2\gamma - \epsilon < 1$, and at both ends simultaneously if $2\gamma - \epsilon = 1$. For the case of a free embedded fibre end, $\epsilon = 0$, and the criterion equation (31) is reduced to that given by Leung and Li (1991). Fig. 5 shows the distribution of the interfacial shear stress for the three cases.

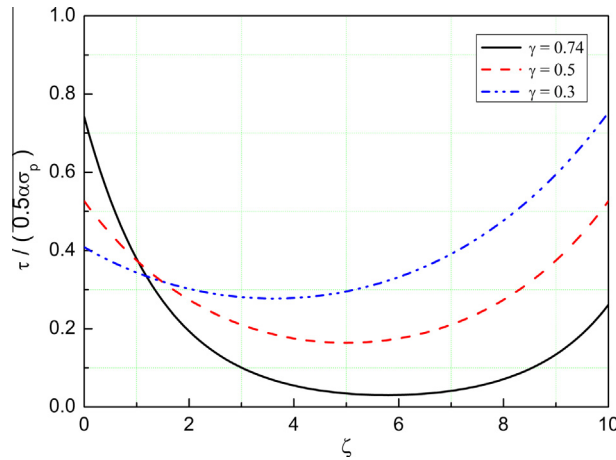


Fig. 5. The distribution of the interfacial shear stress for three different cases ($l = 10$).

4. Solution for damage evolution regime

After interfacial damage initiates, damage process zone will grow and evolve progressively during the fibre pull-out. It can be obtained from Eq. (1)

$$\frac{d\delta}{dz} = \frac{1}{(1-D)K_0} \frac{d\tau}{dz} \tag{32}$$

Substitution of Eq. (10) into Eq. (32), and then into Eq. (19) results in the governing equation for the damage process zone

$$\frac{d^2 \sigma_f(z)}{dz^2} = \frac{2 \left(\frac{a^2}{b^2 - a^2} + \frac{E_A^m}{E_A^f} \right)}{a^2 \left[\frac{E_A^m}{2G_A^f} \left[\frac{l}{a} I(r) \right] + \frac{E_A^m}{2G_A^m} \left[\left(\frac{b^2}{r^2} - 1 \right) \frac{r}{a} O(r) \right] + \frac{E_A^m}{a(1-D)K_0} \right]} \left\{ \sigma_f(z) - \frac{1}{\left[1 + \frac{E_A^m}{E_A^f} \left(\frac{b^2}{a^2} - 1 \right) \right]} \sigma_p - \sigma_T \right\} \tag{33}$$

In Eq. (33), the damage variable D is loading history dependent, and is a function of z due to different shear separations $\delta^{max}(z)$ (and thus different degrees of interfacial softening) in the damage process zone. So the interfacial damage zone is an inhomogeneous elastic interface in terms of the residual interfacial stiffness and strength, and the exact analytical solution of Eq. (33) is generally not available.

Study of the bilinear cohesive traction-separation law provides an idea to find an approximate analytical solution of the interfacial damage and debonding problem. As shown in Fig. 2, the cohesive shear stress due to the interfacial damage, $\tau(\delta^{max})$, is equal to the shear stress predicted by the initial elastic traction-separation behaviour for the current separation without damage, $K_0\delta^{max}$, minus a virtual shear stress, $K_2(\delta^{max} - \delta_0)$. So, the damage behaviour may be approximated by superposition of two elastic systems without damage: one is the initial elastic system

characterised by K_0 ; and the other is a virtual elastic system characterised by K' . This idea is depicted in the schematic diagram Fig. 6.

As illustrated in Fig. 6, the shear stress in the interfacial damage zone is modelled by superposing a shear stress given by the initial linear elastic traction-separation behaviour without damage with an additional shear stress component from the virtual elastic system. It is assumed that the virtual elastic stress system to be superposed does not change the shear stress in the elastic zone nor the separation but affects the stress distribution in the damage process zone only.

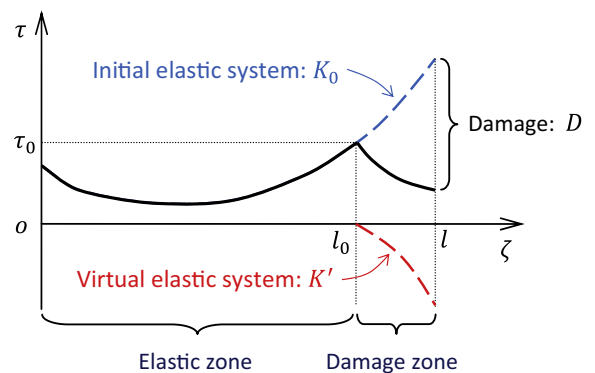


Fig. 6. Schematic diagram showing the idea of approximating interfacial damage by superposition of two elastic systems.

The virtual elastic stress system satisfies the governing equation:

$$\frac{d^2 \sigma_f}{d\zeta^2} = \beta^2 (\sigma_f - \gamma \sigma_0) \tag{34}$$

$$\tau_a = -\frac{1}{2} \frac{d\sigma_f}{d\zeta} \tag{35}$$

where the dimensionless parameter β is obtained from the expression of α by directly replacing K_0 with K' .

For the interfacial damage initiates from the left end (the embedded end), the virtual stress system within the left damage zone ($0 \leq \zeta \leq l_0^L$) satisfies the following boundary conditions:

$$\sigma_f(\zeta = 0) = 0, \quad \text{and} \quad \tau_a(\zeta = l_0^L) = 0 \tag{36}$$

which assures that the virtual stress system satisfies the boundary condition at the embedded end and the damage initiation condition at the right end of the damage zone.

Substituting the boundary conditions equation (36) into Eqs. (34) and (35) yields the solution for the virtual stress system in the left damage zone ($0 \leq \zeta \leq l_0^L$) as

$$\sigma_f = \hat{\sigma}_0^L \left[1 - \frac{\text{Cosh}[\beta(\zeta - l_0^L)]}{\text{Cosh}(\beta l_0^L)} \right]$$

$$\tau_a = \frac{\beta \hat{\sigma}_0^L}{2} \frac{\text{Sinh}[\beta(\zeta - l_0^L)]}{\text{Cosh}(\beta l_0^L)} \tag{37}$$

where $\hat{\sigma}_0^L$ needs to be determined by satisfying the damage evolution law at the left end ($\zeta = 0$) of the damage zone.

If the interfacial damage initiates from the right end (the loaded end), the virtual stress system within the right damage zone ($l_0^R < \zeta < l$) satisfies the following boundary conditions:

$$\sigma_f(\zeta = l_0^R) = 0, \quad \text{and} \quad \tau_a(\zeta = l_0^R) = 0 \tag{38}$$

which assures that the stress in the left elastic zone is not affected by the virtual stress system.

Then the solution for the virtual stress system in the right damage zone ($l_0^R < \zeta < l$) can be given as

$$\sigma_f = \hat{\sigma}_0^R \left\{ 1 - \text{Cosh}[\beta(\zeta - l_0^R)] \right\}$$

$$\tau_a = \frac{\beta \hat{\sigma}_0^R}{2} \text{Sinh}[\beta(\zeta - l_0^R)] \tag{39}$$

where $\hat{\sigma}_0^R$ needs to be determined by satisfying the damage evolution law at the right end ($\zeta = l$) of the damage zone.

Define the following four critical values

$$\sigma_0^L = \frac{2K_0 \delta_0}{\omega(\zeta = 0, l, \alpha)}, \quad \sigma_1^L = \frac{2K_0 \delta_1}{\omega(\zeta = 0, l, \alpha)}, \quad \sigma_0^R$$

$$= \frac{2K_0 \delta_0}{\omega(\zeta = l, l, \alpha)}, \quad \text{and} \quad \sigma_1^R = \frac{2K_0 \delta_1}{\omega(\zeta = l, l, \alpha)} \tag{40}$$

where the subscripts L and R denote the left end ($\zeta = 0$) and the right end ($\zeta = l$), respectively. σ_0^L and σ_1^L are the applied loads when the interfacial shear separation at the left end ($\zeta = 0$) of the initial elastic system reaches δ_0 and δ_1 , respectively, and σ_0^R and σ_1^R are the applied loads when the interfacial shear separation at the right end ($\zeta = l$) of the initial elastic system reaches δ_0 and δ_1 , respectively. It should be noted that once a failure zone initiates in the cohesive interface during the fibre pull-out, the effective length l' , over which the shear stress is transferred, should be used in calculating the corresponding loads by using Eq. (40).

Depending on the geometrical and mechanical properties of the system, the four critical values may be in different orders, and hence there are various scenarios that the interfacial damage and debonding may initiate from different ends (the embedded end and/or the loaded end) in different sequences of events. In this paper, solutions of the stress distributions for the following two scenarios are given:

Scenario 1: $\sigma_0^R < \sigma_1^R < \sigma_0^L < \sigma_1^L$.

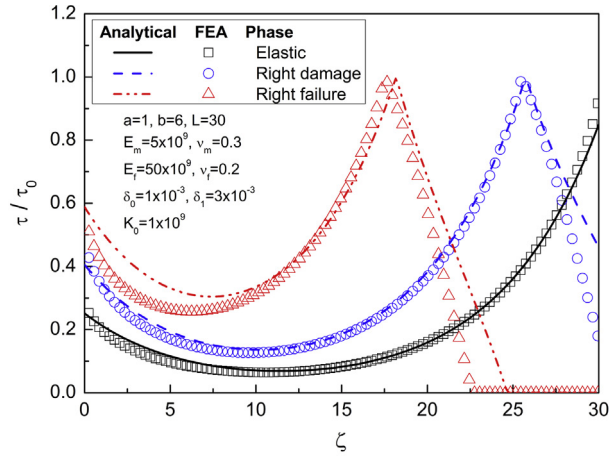
Scenario 2: $\sigma_0^L < \sigma_1^L < \sigma_0^R < \sigma_1^R$.

The details of the solutions for the above two scenarios are given in Appendix A. The solutions for other scenarios can be obtained by following the same solution procedure.

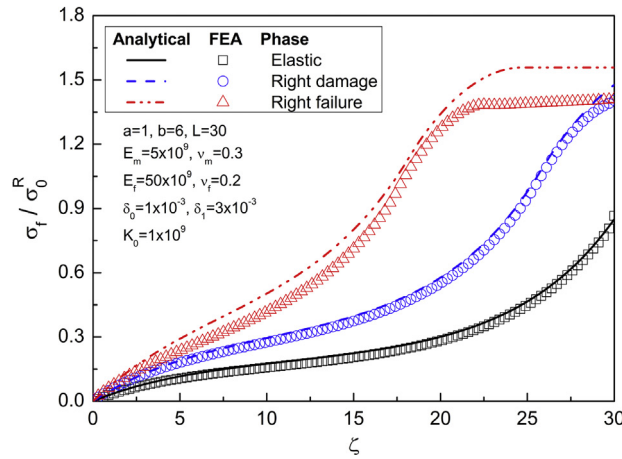
4.1. Scenario 1: damage initiates at right end ($\zeta = l$)

As determined by Eq. (31), interfacial damage will initiate at the right end if $2\gamma - \epsilon < 1$. For this case, after the initial elastic deformation stage, the damage zone initiates at the right end where the interfacial separation reaches δ_0 , and grows leftwards with further loading. When the interfacial separation reaches δ_1 and the cohesive shear traction is reduced to zero, the interfacial failure (debonding) initiates at the right end and grows leftwards. The detailed solutions for the cohesive interface in different stages of deformation are given in Appendix A.1.

Fig. 7(a) and (b) show, respectively, the distributions of the interfacial shear stress and the average axial stress along the fibre at different stages with the left end face of the fibre free from the matrix ($\epsilon = 0$). For the modelled system, $2\gamma - \epsilon = 0.444 < 1$. The finite element modelling of the fibre pullout has been conducted and the results are shown in Fig. 7 for comparison. The geometrical and mechanical parameters for the finite element modelling are given in the inset of Fig. 7. In this study, K' is assumed to equal K_2 . The finite element calculations of the shear traction in the cohesive interface and the average axial stress in the fibre are plotted in Fig. 7. The analytical predictions are in good agreement with the finite element calculations at the elastic stage. When a right damage zone develops, the analytical prediction of the shear stress within the damage zone is larger than the finite element result near the left end of the damage zone, which results in a little larger prediction of the axial stress in the fibre compared with the finite element prediction. Overall, the analytical predictions compare satisfactorily well to the finite element calculations.



(a) The interfacial shear stress.



(b) The average axial stress along the fibre.

Fig. 7. Comparison of the analytical solution to the FE model calculations for the case that damage initiates from the right end: (a) the interfacial shear stress; and (b) the average axial stress along the fibre.

4.2. Scenario 2: damage initiates at left end ($\zeta = 0$)

As determined by Eq. (31), interfacial damage will initiate at the left end if $2\gamma - \epsilon > 1$. For this case, after the initial elastic deformation stage, the damage zone initiates at the left end where the interfacial separation reaches δ_0 , and grows rightwards. When the interfacial separation reaches δ_1 and the cohesive shear traction is reduced to zero, the interfacial failure (debonding) initiates at the left end and grows rightwards. The detailed solutions for the cohesive interface in different stages of deformation are given in Appendix A.2.

Fig. 8(a) and (b) show, respectively, the distributions of the interfacial shear stress and the average axial stress in the fibre at different stages with the left end face of the fibre free from the matrix ($\epsilon = 0$). The finite element analysis results have been plotted for comparison. The parameters used are listed in the inset of Fig. 8(a). For the

modelled system, $2\gamma - \epsilon = 1.54 > 1$. Overall, the analytical predictions compare satisfactorily well to the finite element calculations.

4.3. The maximum fibre pull-out force

For the case of interfacial damage initiates at the right end and the embedded fibre length l is long enough, the maximum pull-out force (stress) is given by

$$\sigma_f^{max} = 2K_0\delta_1 \left\{ \frac{\text{Sinh}(\alpha l)}{\alpha \{ \text{Cosh}(\alpha l) - \epsilon - \gamma [\text{Cosh}(\alpha l) - 1] \}} - \frac{\text{Cosh}[\beta(l - l_0^R)] - 1}{\beta \text{Sinh}[\beta(l - l_0^R)]} \right\} \quad (41)$$

For the case of interfacial damage initiates at the left end, the maximum pull-out force is

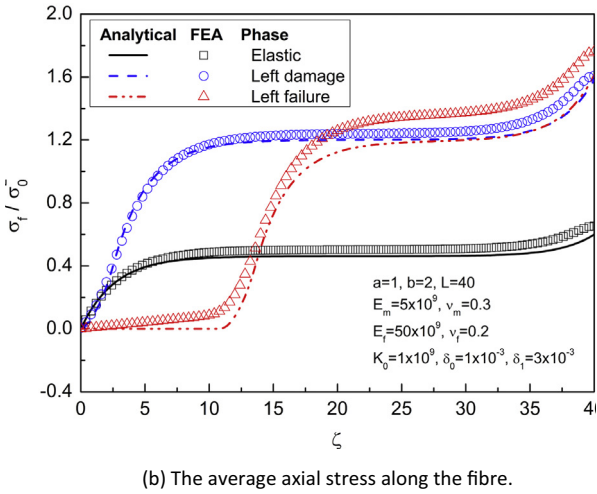
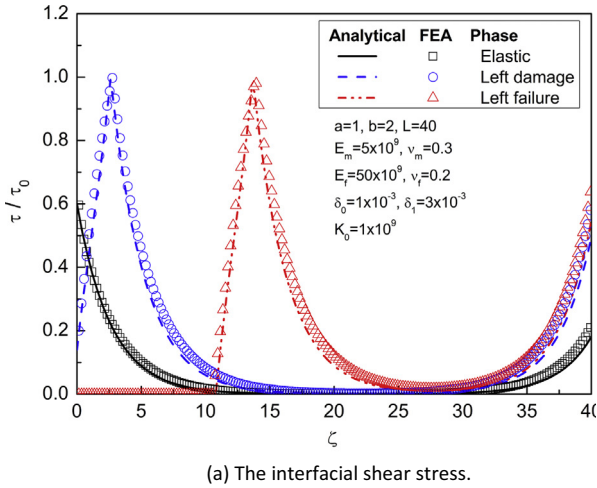


Fig. 8. Comparison of the analytical solution to the FE model calculation for the case that damage initiates from the left end: (a) the interfacial shear stress, and (b) the average axial stress along the fibre.

$$\sigma_f^{max} = 2K_0\delta_1 \left\{ \frac{\text{Sinh}(\alpha l)}{\alpha\{1 - \epsilon\text{Cosh}(\alpha l) - \gamma[1 - \text{Cosh}(\alpha l)]\}} - \frac{\text{Cosh}(\beta l_0^l) - 1}{\beta\text{Sinh}(\beta l_0^l)} \right\} \quad (42)$$

The maximum pull-out force, σ_f^{max} , given by Eqs. (41) and (42) increases with the embedded fibre length. As the embedded fibre length l approaches infinity, we have

$$\lim_{l \rightarrow \infty} (l - l_0^R) = \lim_{l \rightarrow \infty} l_0^L = \frac{1}{\alpha} \ln \frac{\delta_1}{\delta_0} \quad (43)$$

Then, Eqs. (41) and (42) yield, respectively,

$$\lim_{l \rightarrow \infty} \sigma_f^{max} = 2K\delta_1 \left\{ \frac{1}{\alpha(1 - \gamma)} - \frac{\text{Cosh}\left[\frac{\beta}{\alpha} \ln\left(\frac{\delta_1}{\delta_0}\right)\right] - 1}{\beta\text{Sinh}\left[\frac{\beta}{\alpha} \ln\left(\frac{\delta_1}{\delta_0}\right)\right]} \right\} \quad (44)$$

$$\lim_{l \rightarrow \infty} \sigma_f^{max} = 2K\delta_1 \left\{ \frac{1}{\alpha(\gamma - \epsilon)} - \frac{\text{Cosh}\left[\frac{\beta}{\alpha} \ln\left(\frac{\delta_1}{\delta_0}\right)\right] - 1}{\beta\text{Sinh}\left[\frac{\beta}{\alpha} \ln\left(\frac{\delta_1}{\delta_0}\right)\right]} \right\} \quad (45)$$

Fig. 9 shows the maximum fibre pull-out force (Eq. (41)) as a function of the embedded fibre length for the case of $\epsilon = 0$. The parameters listed in the inset of Fig. 7 are used. It can be seen that the maximum pull-out force increases significantly with the embedded length l when the embedded length is short, and rapidly approaches its limit at a certain embedded length. After that, further increase in the embedded fibre length leads to very limited increase in the maximum fibre pull-out force. So, for a given material system, there is a critical effective embedded fibre length at which the load transfer efficiency of the fibre is nearly saturated. The critical effective length can be obtained by solving Eq. (41) or Eq. (42) with a given maximum pull-out force. It needs to be emphasised that if there is a strong interfacial friction between the matrix and the debonded fibre (Nairn, 2000), which is not considered in this analysis, the relation between the maximum pull-out force and the embedded fibre length should be different from that shown in Fig. 9.

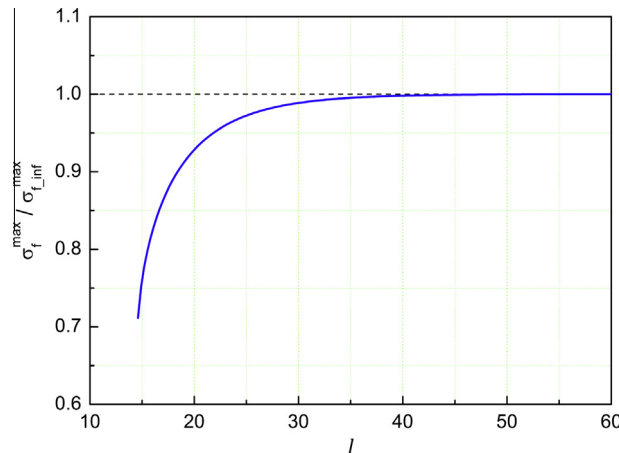


Fig. 9. The maximum fibre pull-out force as a function of the embedded fibre length.

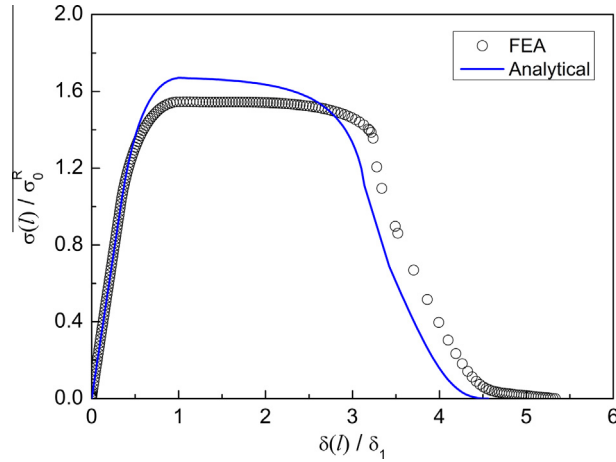


Fig. 10. Comparison of the predicted fibre pull-out curves.

4.4. The fibre pull-out curve

From the solutions for different stages of deformation, the fibre pull-out curve can be derived. Fig. 10 compares the pull-out curves ($\epsilon = 0$) predicted by the analytical solution and the finite element model by using the parameters listed in Fig. 7. In Fig. 10, the pull-out force $\sigma_f(l)$ (the axial stress in the fibre at the loaded end) is plotted as a function of the interfacial separation at the loaded end ($\zeta = l$). For the analytical model, the shear separation within the interfacial failure zone (debonded zone) is approximated as

$$\delta(\zeta) \approx \delta_1 + \frac{\sigma_f^{\max} - \sigma_f(l)}{E_f} (\zeta - l) \quad (l \leq \zeta \leq L) \quad (46)$$

Compared with the finite element prediction, the analytical model overestimates the maximum pull-out force. One reason is due to the one-dimensional characteristics in the simplifications and assumptions adopted in the shear-lag model, while the finite element model is a 3-D simulation and the stress concentration effect may cause earlier damage initiation. Another reason is that the interfacial softening due to damage is approximately modelled by assuming that the virtual stress system does not affect the deformation (interfacial separation) and the damage evolution law is met only at the right and left ends of the damage zone in the approximate analytical model. This may underestimate the interfacial damage and softening, and thus overestimate the shear stress and the pull-out force, as indicated by the results shown in Fig. 7. Overall, the approximate analytical model predicts the stress distributions at different interfacial deformation stages and the fibre pull-out behaviour satisfactorily well.

5. Comparison to experimental results

The stress-transfer characteristics in fragmentation processes in carbon fibre/epoxy resin systems has been studied by using the technique of Laser Raman spectroscopy (Melanitis et al., 1993). A set of fragmentation tests on a short high-modulus carbon fibre embedded in epoxy resin were conducted to obtain the stress distribution along the

fibre at different levels of applied strain. Details about the experimental procedures and results are given in the literature (Melanitis et al., 1993).

Fig. 11 compares the measured fibre strain along the length of the fibre at an applied strain of 0.6% to the predictions of the shear-lag analysis. The mechanical properties and geometries of the fibre/matrix system (Melanitis et al., 1993; Nairn, 2004) and the interfacial cohesive properties used in the analysis are listed in the inset of Fig. 11. The experimental measurements showed that the interfacial shear stress reached a maximum at the bonded fibre ends and decayed to zero at the middle of the fibre. The average maximum interfacial shear stress at the applied strain of 0.6% was 36.7 MPa. This maximum shifted inwards along the fibre fragment and decreased as the applied strain increased. In the fragmentation test, the applied strain was transferred to the fibre through the matrix and both end faces of the fibre were free from the matrix. To model the fragmentation test, we first set the boundary condition parameter $\epsilon = 1$ in Eq. (24), and apply a load σ_p to the right end ($z = 2.8$ mm) of the

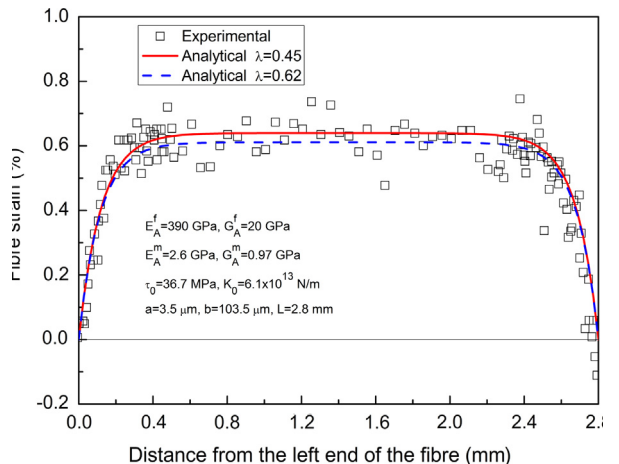


Fig. 11. Comparison of analytical predictions to experimental results of the fibre strain distribution.

fibre to produce a maximum shear stress of 36.7 MPa at both ends of the fibre by using the elastic pull-out solution equation (25). The fibre axial stress in the fragmentation test is then obtained by superposing the pull-out solution with a constant axial stress to produce the zero net axial stress at both ends (free from the matrix) of the fibre. It can be seen from Fig. 11 that the model predictions with using the interfacial cohesive properties fit the experimental data satisfactorily well.

6. Concluding remarks

We have derived the governing equations of a shear-lag model with a cohesive fibre–matrix interface which is modelled by a bilinear cohesive traction-separation law. Analytical solutions for the distribution and evolution of the interfacial shear stress and the axial stress in the fibre during the fibre pull-out have been obtained.

The analytical solution provides a unified expression for the case that the embedded fibre end face is fully bonded with or completely free from the matrix. The accurate solution for the cohesive interface in the initial linear elastic deformation regime is reduced to the result of the classical shear-lag model when the interfacial shear stiffness times the fibre radius is far greater than the axial tensile modulus of the matrix. In addition, the function proposed for the assumed shear stress distribution in the matrix fixes the problem of zero shear-lag parameter when b/a approaches infinity, enabling the shear-lag analysis to deal with low fibre volume fractions.

Interfacial damage and softening are approximated by superposing two elastic stress systems and requiring the damage evolution law to be met at the two ends of the damage process zone, and approximate analytical solutions are obtained. Depending on the geometrical and mechanical properties of the fibre–matrix system, interfacial damage and debonding may occur from different ends of the fibre in different sequences of events.

The maximum fibre pull-out force increases with the embedded fibre length. There is a critical embedded fibre length that the load transfer efficiency of the fibre is nearly saturated, beyond which, the increase in the maximum fibre pull-out force is insignificant.

Compared with the cohesive finite element calculations, the approximate analytical solutions underestimate the interfacial shear stress, and hence overestimate the axial stress in the fibre when interfacial damage and debonding occur. However, considering the one-dimensional characteristics of the shear-lag analysis, the analytical solutions generally agree well with the finite element calculations, and provide a simple method for the analysis of the interfacial damage and debonding during fibre pull-out. The analytical solutions with using appropriate interfacial cohesive properties fit the experimental results satisfactorily well.

Acknowledgements

ZC thanks CSIRO for granting permission to publish this work. The authors would like to thank Prof. John A. Nairn

and an anonymous reviewer for their valuable comments and constructive suggestions to help improve this paper.

Appendix A. Solution for interfacial debonding

A.1. Scenario 1: damage initiates at right end ($\zeta = l$)

As determined by Eq. (31), interfacial damage will initiate from the right end if $2\gamma - \epsilon < 1$. For this case, the cohesive fibre–matrix interface may experience the following stages during the fibre pull-out if $\sigma_0^R < \sigma_1^R < \sigma_0^L < \sigma_1^L$.

Stage 1: fully elastic deformation ($0 \leq \sigma \leq \sigma_0^R$).

The solution for the whole linear elastic cohesive interface ($0 \leq \zeta \leq l$) is

$$\sigma_f = \sigma \varphi(\zeta, l, \alpha) \quad \tau_a = -\frac{\sigma}{2} \omega(\zeta, l, \alpha) \quad \delta = \frac{\sigma}{2K_0} \omega(\zeta, l, \alpha) \quad (A.1)$$

where σ is the applied load, and $\sigma_0^R = \frac{2K_0 \delta_0}{\omega(l, \alpha)} = \frac{2K_0 \delta_0 \text{Sinh}(\alpha l)}{\alpha \{ \text{Cosh}(\alpha l) - \epsilon - \gamma [\text{Cosh}(\alpha l) - 1] \}}$.

Stage 2: damage zone initiates from right end ($\sigma_0^R \leq \sigma \leq \sigma_1^R$).

The cohesive interface consists of a left linear elastic zone ($0 \leq \zeta \leq l_0^R$) and a right damage process zone ($l_0^R \leq \zeta \leq l$). σ_1^R represents the applied load when the separation at the right end ($\zeta = l$) of the initial elastic system reaches δ_1 , and is given by

$$\sigma_1^R = \frac{2K_0 \delta_1}{\omega(l, \alpha)} = \frac{2K_0 \delta_1 \text{Sinh}(\alpha l)}{\alpha \{ \text{Cosh}(\alpha l) - \epsilon - \gamma [\text{Cosh}(\alpha l) - 1] \}}$$

For the left linear elastic zone ($0 \leq \zeta \leq l_0^R$), the solution is given by Eq. (A.1).

The solution for the right damage zone ($l_0^R \leq \zeta \leq l$) is given by

$$\begin{aligned} \sigma_f &= \sigma \varphi(\zeta, l, \alpha) + \hat{\sigma}_0^R \{ 1 - \text{Cosh}[\beta(\zeta - l_0^R)] \} \\ \tau_a &= -\frac{\sigma}{2} \omega(\zeta, l, \alpha) + \frac{\beta \hat{\sigma}_0^R}{2} \text{Sinh}[\beta(\zeta - l_0^R)] \\ \delta &= \frac{\sigma}{2K_0} \omega(\zeta, l, \alpha) \end{aligned} \quad (A.2)$$

where $\hat{\sigma}_0^R$ is determined by satisfying the damage evolution law equation (1) at $\zeta = l$, i.e.

$$\tau(\zeta = l) = K_1 [\delta_1 - \delta(\zeta = l)] \quad (A.3)$$

which results in

$$\hat{\sigma}_0^R = \frac{2[K_2 \delta(\zeta = l) - K_1 \delta_1]}{\beta \text{Sinh}[\beta(l - l_0^R)]} \quad (A.4)$$

The applied load at the right end is

$$\sigma_f(\zeta = l) = \sigma - \hat{\sigma}_0^R \{ \text{Cosh}[\beta(l - l_0^R)] - 1 \} \quad (A.5)$$

For a given l_0 (exactly l_0^R here), i.e. when the right damage zone evolves leftwards to l_0 , the corresponding load, σ , is given by the damage initiation criterion $\tau(\zeta = l_0^R) = \tau_0$ as

$$\sigma = \frac{2\tau_0 \text{Sinh}(\alpha l)}{\alpha \{ \text{Cosh}(\alpha l_0) - \epsilon \text{Cosh}[\alpha(l_0 - l)] - \gamma [\text{Cosh}(\alpha l_0) - \text{Cosh}[\alpha(l_0 - l)]] \}} \tag{A.6}$$

Or, inversely, for a given $(\sigma_0^R \leq \sigma \leq \sigma_1^R)$, l_0 is obtained by solving Eq. (A.6) as

$$l_0^{R,L} = \frac{1}{\alpha} \ln \frac{\frac{2\tau_0}{\alpha\sigma} \text{Sinh}(\alpha l) \pm \sqrt{\left[\frac{2\tau_0}{\alpha\sigma} \text{Sinh}(\alpha l)\right]^2 - [1 - \gamma + (\gamma - \epsilon)e^{-\alpha l}][1 - \gamma + (\gamma - \epsilon)e^{\alpha l}]}}{[1 - \gamma + (\gamma - \epsilon)e^{-\alpha l}]} \tag{A.7}$$

Stage 3: failure initiates at right end ($\sigma = \sigma_1^R$).

As the interfacial shear separation at right end reaches the critical value δ_1 , i.e. $\delta(\zeta = l) = \delta_1$, the interfacial failure (debonding) initiates at the right end. The solution is the same as that for Stage 2 with $\hat{\sigma}_1^R$ given by

$$\hat{\sigma}_1^R = \frac{2[K_2\delta(\zeta = l) - K_1\delta_1]}{\beta \text{Sinh}[\beta(l - l_0^R)]} = \frac{2[K_2\delta_1 - K_1\delta_1]}{\beta \text{Sinh}[\beta(l - l_0^R)]} = \frac{2K_0\delta_1}{\beta \text{Sinh}[\beta(l - l_0^R)]} \tag{A.8}$$

Stage 4: right failure zone grows leftwards

During this stage, the cohesive interface consists of a left linear elastic zone ($0 < \zeta < l_0^R$), a middle damage zone ($l_0^R < \zeta < l'$), and a right failure zone ($l' < \zeta < l$).

The solutions for the elastic zone and the damage zone can be obtained directly by replacing l with the effective embedded length l' as:

The left linear elastic zone ($0 < \zeta < l_0^R$)

$$\sigma_f = \sigma\varphi(\zeta, l', \alpha) \quad \tau_a = -\frac{\sigma}{2}\omega(\zeta, l', \alpha) \quad \delta = \frac{\sigma}{2K_0}\omega(\zeta, l', \alpha) \tag{A.9}$$

The middle damage zone ($l_0^R < \zeta < l'$)

$$\sigma_f = \sigma\varphi(\zeta, l', \alpha) + \hat{\sigma}_1^R \{1 - \text{Cosh}[\beta(\zeta - l_0^R)]\}$$

$$\tau_a = -\frac{\sigma}{2}\omega(\zeta, l', \alpha) + \frac{\beta\hat{\sigma}_1^R}{2} \text{Sinh}[\beta(\zeta - l_0^R)]$$

$$\delta = \frac{\sigma}{2K_0}\omega(\zeta, l', \alpha) \tag{A.10}$$

where $\hat{\sigma}_1^R = \frac{2K_0\delta_1}{\beta \text{Sinh}[\beta(l' - l_0^R)]}$, and $\sigma = \frac{2K_0\delta_1 \text{Sinh}(\alpha l')}{\alpha [\text{Cosh}(\alpha l') - \epsilon - \gamma(\text{Cosh}(\alpha l') - 1)]}$, which decreases with l' .

The right failure zone ($l' < \zeta < l$)

$$\sigma_f = \sigma_f(\zeta = l') = \frac{2K_0\delta_1 \text{Sinh}(\alpha l')}{\alpha [\text{Cosh}(\alpha l') - \epsilon - \gamma(\text{Cosh}(\alpha l') - 1)]} \tag{A.11}$$

$$\tau_a = 0$$

Stage 5: left damage zone initiates and grows rightwards

As the effective embedded length l' decreases, the left damage zone may initiate and grow rightwards. In this stage, the cohesive interface consists of a left damage zone ($0 < \zeta < l_0^L$), a middle elastic zone ($l_0^L < \zeta < l_0^R$), a right

fully developed damage zone ($l_0^R < \zeta < l$), and a right failure zone ($l' < \zeta < l$).

The solution for the left damage zone ($0 < \zeta < l_0^L$) is

$$\sigma_f = \sigma\varphi(\zeta, l', \alpha) + \hat{\sigma}_0^L \left[1 - \frac{\text{Cosh}[\beta(\zeta - l_0^L)]}{\text{Cosh}(\beta l_0^L)}\right]$$

$$\tau_a = -\frac{\sigma}{2}\omega(\zeta, l', \alpha) + \frac{\beta\hat{\sigma}_0^L}{2} \frac{\text{Sinh}[\beta(\zeta - l_0^L)]}{\text{Cosh}(\beta l_0^L)}$$

$$\delta = \frac{\sigma}{2K_0}\omega(\zeta, l', \alpha) \tag{A.12}$$

where $\hat{\sigma}_0^L = \frac{2[K_1\delta_1 - K_2\delta(\zeta=0)]\text{Coth}(\beta l_0^L)}{\beta}$.

The solution for the middle elastic zone ($l_0^L < \zeta < l_0^R$) is

$$\sigma_f = \sigma\varphi(\zeta, l', \alpha) + \hat{\sigma}_{00}^L \quad \tau_a = -\frac{\sigma}{2}\omega(\zeta, l', \alpha) \quad \delta = \frac{\sigma}{2K_0}\omega(\zeta, l', \alpha) \tag{A.13}$$

where $\hat{\sigma}_{00}^L = \hat{\sigma}_0^L \left[1 - \frac{1}{\text{Cosh}(\beta l_0^L)}\right]$.

The solution for the right damage zone ($l_0^R < \zeta < l'$) is

$$\sigma_f = \sigma\varphi(\zeta, l', \alpha) + \hat{\sigma}_{00}^L + \hat{\sigma}_1^R \{1 - \text{Cosh}[\beta(\zeta - l_0^R)]\}$$

$$\tau_a = -\frac{\sigma}{2}\omega(\zeta, l', \alpha) + \frac{\beta\hat{\sigma}_1^R}{2} \text{Sinh}[\beta(\zeta - l_0^R)]$$

$$\delta = \frac{\sigma}{2K_0}\omega(\zeta, l', \alpha) \tag{A.14}$$

The solution for the right failure zone ($l' < \zeta < l$) is

$$\sigma_f = \sigma_f(\zeta = l')$$

$$= \frac{2K_0\delta_1 \text{Sinh}(\alpha l')}{\alpha [\text{Cosh}(\alpha l') - \epsilon - \gamma(\text{Cosh}(\alpha l') - 1)]} \tag{A.15}$$

$$+ \hat{\sigma}_{00}^L + \hat{\sigma}_1^R \{1 - \text{Cosh}[\beta(l' - l_0^R)]\}$$

$$\tau_a = 0$$

Stage 6: left and right damage zones merge before failure initiates at the left end

In this stage, the left and right damage zones merge. The cohesive interface consists of a left damage zone ($0 < \zeta < l_0$), a right damage zone ($l_0 < \zeta < l$), and a right failure zone ($l' < \zeta < l$).

The solution for the left part of the damage zone ($0 < \zeta < l_0$) is

$$\begin{aligned} \sigma_f &= \sigma\varphi(\zeta, l', \alpha) + (\tilde{\sigma}_1^L + c_1 e^{\beta\zeta} + c_2 e^{-\beta\zeta}) \\ \tau_a &= -\frac{\sigma}{2}\omega(\zeta, l', \alpha) - \frac{\beta}{2}(c_1 e^{\beta\zeta} - c_2 e^{-\beta\zeta}) \\ \delta &= \frac{\sigma}{2K_0}\omega(\zeta, l', \alpha) \end{aligned} \tag{A.16}$$

where

$$\begin{aligned} c_1 &= \frac{B - Ae^{-\beta l_0}}{e^{\beta l_0} - e^{-\beta l_0}} \quad c_2 = \frac{B - Ae^{\beta l_0}}{e^{\beta l_0} - e^{-\beta l_0}} \quad \tilde{\sigma}_1^L = -\frac{2B - Ae^{\beta l_0} - Ae^{-\beta l_0}}{e^{\beta l_0} - e^{-\beta l_0}} \\ A &= \frac{2[K_1\delta_1 - K_2\delta(\zeta=0)]}{\beta} \quad B = \frac{2[K_1\delta_1 - K_2\delta(\zeta=l_0)]}{\beta} \end{aligned}$$

The solution for the right part of the damage zone ($l_0 < \zeta < l$) is

$$\begin{aligned} \sigma_f &= \sigma\varphi(\zeta, l', \alpha) + (\tilde{\sigma}_0^R + c_3 e^{\beta\zeta} + c_4 e^{-\beta\zeta}) \\ \tau_a &= -\frac{\sigma}{2}\omega(\zeta, l', \alpha) - \frac{\beta}{2}(c_3 e^{\beta\zeta} - c_4 e^{-\beta\zeta}) \\ \delta &= \frac{\sigma}{2K_0}\omega(\zeta, l', \alpha) \end{aligned} \tag{A.17}$$

where

$$\begin{aligned} c_3 &= \frac{Fe^{\beta l'} - Ee^{\beta l_0}}{e^{2\beta l'} - e^{2\beta l_0}} \quad c_4 = -\frac{Fe^{-\beta l'} - Ee^{-\beta l_0}}{e^{-2\beta l'} - e^{-2\beta l_0}} \quad \tilde{\sigma}_0^R \\ &= \tilde{\sigma}_1^L + c_1 e^{\beta l_0} + c_2 e^{-\beta l_0} - (c_3 e^{\beta l_0} + c_4 e^{-\beta l_0}) \\ E &= c_1 e^{\beta l_0} - c_2 e^{-\beta l_0} \quad F = -\frac{2K_0\delta_1}{\beta} \end{aligned}$$

Here l_0 is determined by the condition that the shear separation has a minimum at ($\zeta = l_0$) as

$$l_0 = \frac{1}{2\alpha} \ln \frac{(1 + \gamma) - (\epsilon - \gamma)e^{\alpha l'}}{1 + \gamma - (\epsilon - \gamma)e^{-\alpha l'}} \tag{A.18}$$

The solution for the right failure zone ($l' < \zeta < l$) is

$$\begin{aligned} \sigma_f &= \sigma_f(\zeta = l') = \frac{2K_0\delta_1 \text{Sinh}(\alpha l')}{\alpha[\text{Cosh}(\alpha l') - \epsilon - \gamma(\text{Cosh}(\alpha l') - 1)]} + (\tilde{\sigma}_0^R + c_3 e^{\beta l'} + c_4 e^{-\beta l'}) \\ \tau_a &= 0 \end{aligned} \tag{A.19}$$

Stage 7: left failure zone initiates and middle damage zone shrinks

In this stage, a failure zone ($0 < \zeta < l_1^L$) initiates from the left end, and the damage zone ($l_1^L < \zeta < l'$) shrinks until the total interfacial debonding. The solution in Stage

6 is still valid with $A = -2K_0\delta_1/\beta$. And it is easy to express the solution by introducing a new coordinate, with its origin moving rightwards with l_1^L .

A.2. Scenario 2: damage initiates at left end ($\zeta = 0$)

As determined by Eq. (31), interfacial damage will initiate from the left end if $2\gamma - \epsilon > 1$. For this case, the cohesive fibre–matrix interface may experience the following stages during the fibre pull-out.

Stage 1: fully elastic deformation ($0 \leq \sigma \leq \sigma_0^L$).

The solution for the whole linear elastic cohesive interface ($0 \leq \zeta \leq l$) is

$$\sigma_f = \sigma\varphi(\zeta, l, \alpha) \quad \tau_a = -\frac{\sigma}{2}\omega(\zeta, l, \alpha) \quad \delta = \frac{\sigma}{2K_0}\omega(\zeta, l, \alpha) \tag{A.20}$$

where σ is the applied load, and $\sigma_0^L = \frac{2K_0\delta_0}{\omega(0, l, \alpha)} = \frac{2K_0\delta_0 \text{Sinh}(\alpha l)}{\alpha\{1 - \epsilon \text{Cosh}(\alpha l) - \gamma[1 - \text{Cosh}(\alpha l)]\}}$.

Stage 2: damage zone initiates from left end ($\sigma_0^L \leq \sigma \leq \sigma_1^L$).

The cohesive interface consists of a left damage process zone ($0 \leq \zeta \leq l_0^L$) and a right linear elastic zone ($l_0^L \leq \zeta \leq l$). σ_1^L represents the applied load when the interfacial shear separation at the left end ($\zeta = 0$) of the initial elastic system reaches δ_1 , and is given by

$$\sigma_1^L = \frac{2K_0\delta_1}{\omega(0, l, \alpha)} = \frac{2K_0\delta_1 \text{Sinh}(\alpha l)}{\alpha\{1 - \epsilon \text{Cosh}(\alpha l) - \gamma[1 - \text{Cosh}(\alpha l)]\}}$$

The solution for the left damage zone ($0 \leq \zeta \leq l_0^L$) is given by

$$\begin{aligned} \sigma_f &= \sigma\varphi(\zeta, l, \alpha) + \tilde{\sigma}_0^L \left[1 - \frac{\text{Cosh}[\beta(\zeta - l_0^L)]}{\text{Cosh}(\beta l_0^L)} \right] \\ \tau_a &= -\frac{\sigma}{2}\omega(\zeta, l, \alpha) + \frac{\beta\tilde{\sigma}_0^L}{2} \frac{\text{Sinh}[\beta(\zeta - l_0^L)]}{\text{Cosh}(\beta l_0^L)} \\ \delta &= \frac{\sigma}{2K_0}\omega(\zeta, l, \alpha) \end{aligned} \tag{A.21}$$

where $\tilde{\sigma}_0^L = \frac{2[K_1\delta_1 - K_2\delta(\zeta=0)]\text{Coth}(\beta l_0^L)}{\beta}$.

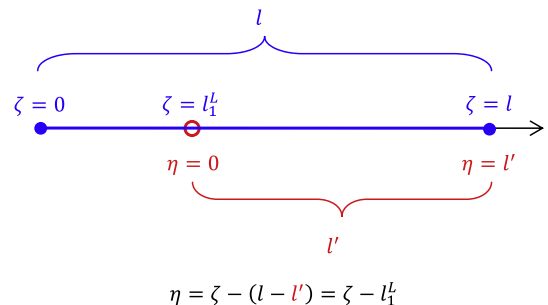


Fig. 12. A new moving coordinate system.

The solution for the right elastic zone ($l_0^t \leq \zeta \leq l$) is

$$\begin{aligned} \sigma_f &= \sigma\varphi(\zeta, l, \alpha) + \hat{\sigma}_{00}^L \\ \tau_a &= -\frac{\sigma}{2}\omega(\zeta, l, \alpha) \\ \delta &= \frac{\sigma}{2K_0}\omega(\zeta, l, \alpha) \end{aligned} \tag{A.22}$$

where $\hat{\sigma}_{00}^L = \hat{\sigma}_0^L \left[1 - \frac{1}{\text{Cosh}(\beta l_0^t)} \right]$.

Stage 3: failure initiates at left end ($\sigma = \sigma_1^L$).

As the interfacial shear separation at the left end reaches the critical value δ_1 , i.e. $\delta(\zeta = 0) = \delta_1$, the interfacial failure (debonding) initiates at the left end. The solution is the same as that for Stage 2 with replacing $\hat{\sigma}_0^L$ with $\hat{\sigma}_1^L$, and $\hat{\sigma}_{00}^L$ with $\hat{\sigma}_{10}^L$ as

$$\begin{aligned} \hat{\sigma}_1^L &= \frac{2[K_1\delta_1 - K_2\delta(\zeta = 0)]\text{Coth}(\beta l_0^t)}{\beta} \\ &= \frac{2[K_1\delta_1 - K_2\delta_1]\text{Coth}(\beta l_0^t)}{\beta} = -\frac{2K_0\delta_1\text{Coth}(\beta l_0^t)}{\beta} \\ \hat{\sigma}_{10}^L &= \hat{\sigma}_1^L \left[1 - \frac{1}{\text{Cosh}(\beta l_0^t)} \right] \end{aligned}$$

Stage 4: left failure zone grows rightwards

During this stage, due to the partial interfacial debonding from the left end, the effective fibre length reduces from the initial length l to l' . It is much convenient to express the solution by introducing a new moving coordinate η as shown in Fig. 12.

The solution for the left failure zone ($0 < \zeta < l - l'$) is

$$\sigma_f = \sigma\epsilon \quad \tau_a = 0 \tag{A.23}$$

The solution for the middle damage zone ($l - l' < \zeta < l - l' + l_0^t$, or equivalently $0 < \eta < l_0^t$) is

$$\begin{aligned} \sigma_f &= \sigma\varphi(\eta, l', \alpha) + \hat{\sigma}_1^L \left[1 - \frac{\text{Cosh}[\beta(\eta - l_0^t)]}{\text{Cosh}(\beta l_0^t)} \right] \\ \tau_a &= -\frac{\sigma}{2}\omega(\eta, l', \alpha) + \frac{\beta\hat{\sigma}_1^L}{2} \frac{\text{Sinh}[\beta(\eta - l_0^t)]}{\text{Cosh}(\beta l_0^t)} \\ \delta &= \frac{\sigma}{2K_0}\omega(\eta, l', \alpha) \end{aligned} \tag{A.24}$$

where $\hat{\sigma}_1^L = \frac{2K_0\delta_1}{\omega(0, l', \alpha)} = \frac{2K_0\delta_1 \text{Sinh}(\alpha l')}{\alpha \{ 1 - e^{\text{Cosh}(\alpha l')} - \gamma [1 - \text{Cosh}(\alpha l')] \}}$, which decreases as l' decreases.

Note, here l_0^t is a function of the effective fibre length l' .

The solution for the right elastic zone ($l_0^t < \eta < l'$) is

$$\sigma_f = \sigma\varphi(\eta, l', \alpha) + \hat{\sigma}_{10}^L$$

$$\begin{aligned} \tau_a &= -\frac{\sigma}{2}\omega(\eta, l', \alpha) \\ \delta &= \frac{\sigma}{2K_0}\omega(\eta, l', \alpha) \end{aligned} \tag{A.25}$$

Stage 5: right damage zone initiates and grows leftwards

In this stage, the cohesive interface consists of a left failure zone ($0 < \zeta < l - l'$), a left damage zone ($0 < \eta < l_0^t$), a middle elastic zone ($l_0^t < \eta < l_0^R$), and a right damage zone ($l_0^R < \eta < l'$).

The solutions for the left failure zone, the left damage zone and the middle elastic zone are the same as those in Stage 4.

The solution for the right damage zone ($l_0^R < \eta < l'$) is

$$\begin{aligned} \sigma_f &= \sigma\varphi(\eta, l', \alpha) + \hat{\sigma}_{10}^L + \hat{\sigma}_0^R \left\{ 1 - \text{Cosh}[\beta(\zeta - l_0^R)] \right\} \\ \tau_a &= -\frac{\sigma}{2}\omega(\eta, l', \alpha) + \frac{\beta\hat{\sigma}_0^R}{2} \text{Sinh}[\beta(\zeta - l_0^R)] \\ \delta &= \frac{\sigma}{2K_0}\omega(\eta, l', \alpha) \end{aligned} \tag{A.26}$$

where $\hat{\sigma}_0^R = \frac{2[K_2\delta(\eta=l') - K_1\delta_1]}{\beta \text{Sinh}[\beta(l' - l_0^R)]}$.

Stage 6: right and left damage zones merge before failure initiates at right end

The solution for the left failure zone ($0 < \zeta < l - l'$) is the same as that in Stage 4.

The solution for the left damage zone ($0 < \eta < l_0$) is

$$\begin{aligned} \sigma_f &= \sigma\varphi(\eta, l', \alpha) + (\tilde{\sigma}_1^L + c_1 e^{\beta\eta} + c_2 e^{-\beta\eta}) \\ \tau_a &= -\frac{\sigma}{2}\omega(\eta, l', \alpha) - \frac{\beta}{2}(c_1 e^{\beta\eta} - c_2 e^{-\beta\eta}) \\ \delta &= \frac{\sigma}{2K_0}\omega(\eta, l', \alpha) \end{aligned} \tag{A.27}$$

where

$$\begin{aligned} c_1 &= \frac{B - Ae^{-\beta l_0}}{e^{\beta l_0} - e^{-\beta l_0}} \quad c_2 = \frac{B - Ae^{\beta l_0}}{e^{\beta l_0} - e^{-\beta l_0}} \quad \tilde{\sigma}_1^L = -(c_1 + c_2) \\ &= -\frac{2B - Ae^{\beta l_0} - Ae^{-\beta l_0}}{e^{\beta l_0} - e^{-\beta l_0}} \end{aligned}$$

$$A = -\frac{2K_0\delta_1}{\beta} \quad B = \frac{2[K_1\delta_1 - K_2\delta(\eta = l_0)]}{\beta}$$

The solution for the right damage zone ($l_0 < \eta < l'$) is

$$\begin{aligned} \sigma_f &= \sigma\varphi(\eta, l', \alpha) + (\tilde{\sigma}_0^R + c_3 e^{\beta\eta} + c_4 e^{-\beta\eta}) \\ \tau_a &= -\frac{\sigma}{2}\omega(\eta, l', \alpha) - \frac{\beta}{2}(c_3 e^{\beta\eta} - c_4 e^{-\beta\eta}) \\ \delta &= \frac{\sigma}{2K_0}\omega(\eta, l', \alpha) \end{aligned} \tag{A.28}$$

where

$$c_3 = \frac{Fe^{\beta l'} - Ee^{\beta l_0}}{e^{2\beta l'} - e^{2\beta l_0}} \quad c_4 = -\frac{Fe^{-\beta l'} - Ee^{-\beta l_0}}{e^{-2\beta l'} - e^{-2\beta l_0}} \quad \tilde{\sigma}_0^R$$

$$= \tilde{\sigma}_1^L + c_1 e^{\beta l_0} + c_2 e^{-\beta l_0} - (c_3 e^{\beta l_0} + c_4 e^{-\beta l_0})$$

$$E = c_1 e^{\beta l_0} - c_2 e^{-\beta l_0} \quad F = \frac{2[K_1 \delta_1 - K_2 \delta(\eta = l')]}{\beta}$$

Stage 7: right failure zone initiates and grows leftwards, and middle damage zone shrinks

In this stage, a failure zone ($l' < \eta < l$) initiates from the right end and grows leftwards, and the middle damage zone ($0 < \eta < l'$) shrinks until total interfacial debonding. The solution in Stage 6 is still valid with $F = -2K_0 \delta_1 / \beta$.

References

- Agnihotri, P.K., Kar, K.K., Basu, S., 2012. Cohesive zone model of carbon nanotube-coated carbon fiber/polyester composites. *Modell. Simul. Mater. Sci. Eng.* 20 (035014), 1–13.
- Aveston, J., Kelly, A., 1973. Theory of multiple fracture of fibrous composites. *J. Mater. Sci.* 8, 352–362.
- Budiansky, B., Hutchinson, J.W., Evans, A.G., 1986. Matrix fracture in fiber-reinforced ceramics. *J. Mech. Phys. Solids* 34, 167–189.
- Chen, Y.L., Liu, B., He, X.Q., Huang, Y., Hwang, K.C., 2010. Failure analysis and the optimal toughness design of carbon nanotube-reinforced composites. *Compos. Sci. Technol.* 70, 1360–1367.
- Clyne, T.W., 1989. A simple development of the shear lag theory appropriate for composites with a relatively small modulus mismatch. *Mater. Sci. Eng. A-Struct. Mater. Prop. Microstruct. Process.* 122, 183–192.
- Cox, H.L., 1952. The elasticity and strength of paper and other fibrous materials. *Br. J. Appl. Phys.* 3, 72–79.
- Frankland, S.J.V., Harik, V.M., 2003. Analysis of carbon nanotube pull-out from a polymer matrix. *Surf. Sci.* 525, L103–L108.
- Frankland, S.J.V., Caglar, A., Brenner, D.W., Griebel, M., 2002. Molecular simulation of the influence of chemical cross-links on the shear strength of carbon nanotube-polymer interfaces. *J. Phys. Chem. B* 106, 3046–3048.
- Frankland, S.J.V., Harik, V.M., Odegard, G.M., Brenner, D.W., Gates, T.S., 2003. The stress-strain behavior of polymer-nanotube composites from molecular dynamics simulation. *Compos. Sci. Technol.* 63, 1655–1661.
- Gao, X.L., Li, K., 2005. A shear-lag model for carbon nanotube-reinforced polymer composites. *Int. J. Solids Struct.* 42, 1649–1667.
- Gao, Y.C., Mai, Y.W., Cotterell, B., 1988. Fracture of fiber-reinforced materials. *J. Appl. Math. Phys. (ZAMP)* 39, 550–572.
- Gurney, C., Hunt, J., 1967. Quasi-static crack propagation. *Proc. Roy. Soc. Lond. Ser. A-Math. Phys. Sci.* 299, 508–524.
- Hsueh, C.H., 1988. Elastic load-transfer from partially embedded axially loaded fiber to matrix. *J. Mater. Sci. Lett.* 7, 497–500.
- Hsueh, C.H., 1992. Interfacial debonding and fiber pull-out stresses of fiber-reinforced composites. 7. Improved analyses for bonded interfaces. *Mater. Sci. Eng. A-Struct. Mater. Prop. Microstruct. Process.* 154, 125–132.
- Hutchinson, J.W., Jensen, H.M., 1990. Models of fiber debonding and pullout in brittle composites with friction. *Mech. Mater.* 9, 139–163.
- Jia, Y., Chen, Z., Yan, W., 2014. A numerical study on carbon nanotube-hybridized carbon fibre pullout. *Compos. Sci. Technol.* 91, 38–44.
- Jiang, L.Y., 2010. A cohesive law for carbon nanotube/polymer interface accounting for chemical covalent bonds. *Math. Mech. Solids* 15, 718–732.
- Jiang, L.Y., Huang, Y., Jiang, H., Ravichandran, G., Gao, H., Hwang, K.C., Liu, B., 2006. A cohesive law for carbon nanotube/polymer interfaces based on the van der Waals force. *J. Mech. Phys. Solids* 54, 2436–2452.
- Kim, J.K., Baillie, C., Mai, Y.W., 1992. Interfacial debonding and fiber pull-out stresses. 1. Critical comparison of existing theories with experiments. *J. Mater. Sci.* 27, 3143–3154.
- Landis, C.M., McMeeking, R.M., 1999. A shear-lag model for a broken fiber embedded in a composite with a ductile matrix. *Compos. Sci. Technol.* 59, 447–457.
- Lawrence, P., 1972. Some theoretical considerations of fiber pull-out from an elastic matrix. *J. Mater. Sci.* 7, 1–6.
- Leung, C.K.Y., Li, V.C., 1991. New strength-based model for the debonding of discontinuous fibers in an elastic matrix. *J. Mater. Sci.* 26, 5996–6010.
- Lu, W.B., Wu, J., Song, J., Hwang, K.C., Jiang, L.Y., Huang, Y., 2008. A cohesive law for interfaces between multi-wall carbon nanotubes and polymers due to the van der Waals interactions. *Comput. Methods Appl. Mech. Eng.* 197, 3261–3267.
- Marshall, D.B., Cox, B.N., Evans, A.G., 1985. The mechanics of matrix cracking in brittle-matrix fiber composites. *Acta Metallur.* 33, 2013–2021.
- McCartney, L.N., 1989. New theoretical-model of stress transfer between fiber and matrix in a uniaxially fiber-reinforced composite. *Proc. Roy. Soc. Lond. Ser. A-Math. Phys. Eng. Sci.* 425, 215–244.
- McCartney, L.N., 1992. Analytical models of stress transfer in unidirectional composites and cross-ply laminates, and their application to the prediction of matrix/transverse cracking. In: Reddy, J.N., Reifsnider, K.L. (Eds.), *Local Mechanics Concepts For Composite Material Systems*, Proc. Iutam Symposium, Blacksburg, Va, pp. 251–282.
- Melanitis, N., Galiotis, C., Tetlow, P.L., Davies, C.K.L., 1993. Monitoring the micromechanics of reinforcement in carbon-fiber epoxy-resin systems. *J. Mater. Sci.* 28, 1648–1654.
- Nairn, J.A., 1997. On the use of shear-lag methods for analysis of stress transfer unidirectional composites. *Mech. Mater.* 26, 63–80.
- Nairn, J.A., 2000. Analytical fracture mechanics analysis of the pull-out test including the effects of friction and thermal stresses. *Adv. Compos. Lett.* 9, 373–383.
- Nairn, J.A., 2004. Generalized shear-lag analysis including imperfect interfaces. *Adv. Compos. Lett.* 13, 263–274.
- Nayfeh, A.H., 1977. Thermo-mechanically induced interfacial stresses in fibrous composites. *Fibre Sci. Technol.* 10, 195–209.
- Nayfeh, A.H., Abdelrahman, W.G., 1998. Micromechanical modeling of load transfer in fibrous composites. *Mech. Mater.* 30, 307–324.
- Shetty, D.K., 1988. Shear-lag analysis of fiber push-out (indentation) tests for estimating interfacial friction stress in ceramic-matrix composites. *J. Am. Cer. Soc.* 71, C107–C109.
- Stang, H., Shah, S.P., 1986. Failure of fiber-reinforced composites by pull-out fracture. *J. Mater. Sci.* 21, 953–957.
- Stang, H., Li, Z., Shah, S.P., 1990. Pullout problem – stress versus fracture mechanical approach. *J. Eng. Mech.-ASCE* 116, 2136–2150.
- Starink, M.J., Syngellakis, S., 1999. Shear lag models for discontinuous composites: fibre end stresses and weak interface layers. *Mater. Sci. Eng. A-Struct. Mater. Prop. Microstruct. Process.* 270, 270–277.
- Zhandarov, S., Pisanova, E., Mader, E., Nairn, J.A., 2001. Investigation of load transfer between the fiber and the matrix in pull-out tests with fibers having different diameters. *J. Adhes. Sci. Technol.* 15, 205–222.
- Zhou, L.M., Kim, J.K., Mai, Y.W., 1992. Interfacial debonding and fiber pull-out stresses. 2. A new model based on the fracture-mechanics approach. *J. Mater. Sci.* 27, 3155–3166.
- Zhou, L.M., Kim, J.K., Mai, Y.W., 1993. Micromechanical characterization of fiber-matrix interfaces. *Compos. Sci. Technol.* 48, 227–236.